TJNN Thai Journal of Nanoscience and Nanotechnology

The Effect of W Dopants on the Physical and Optical Properties and Photocatalytic Activity of ZnO Synthesized by the Co-precipitation Method

Junkrajang Wattana[1,*], Maneerat Songpanit[1], Thanaphon Kansaard[1], Jirayu Tachaworakit[1], Thinnasit Thanathaninruj[1], Chatpong Bangbai[2], and Wanichaya Mekprasart[1]

[1]*School of Integrated Innovative Technology, King Mongkut's Institute of Technology Ladkrabang, Bangkok, 10520, Thailand*

[2]*Department of Science and Mathematics, Faculty of Science and Health Technology, Kalasin University, Kalasin, 46000, Thailand*

Received: 2 May 2025, Revised: 17 June 2025, Accepted: 23 June 2025

Abstract

Due to the wastewater crisis, tungsten (W)-doped ZnO particles were synthesized with varying W dopant concentrations using the co-precipitation method for the enhancement of photocatalysis application, which can reduce the wastewater crisis by the degradation of pollutant molecules occurring during its process. The crystalline and optical properties of the synthesized powders were analyzed by various methods, as well as their photocatalytic performance. Among all conditions, the WZ-5 sample exhibited the lowest band gap energy at 3.11 eV and the highest photocatalytic efficiency, achieving 98.16% degradation within 60 minutes. These results demonstrate that tungsten doping can effectively enhance ZnO photocatalytic activity by promoting better charge carrier separation and extending light absorption, especially in the visible region, making W-doped ZnO a promising material for wastewater treatment applications.

Keywords: W-doped ZnO, Co-precipitation, Physical property, Optical property, Photocatalysis

1. Introduction

Semiconductors are materials that can switch their electrical and optical properties between insulators and conductors by receiving an electromagnetic wavelength, causing electrons to be excited and transfer themselves from the valence band to the conduction band, generating an electron-hole pair in a material. This unique property allows semiconductors to conduct electricity under certain conditions, making them essential for many applications such as electronic devices [1], [2], optoelectronic devices [3], [4], solar cells [5], [6], sensors [7], [8], light-shielding materials [9], [10] and photocatalysts [11], [12]. Due to significant environmental concerns in urban areas, wastewater management has become a critical issue, as contaminated water poses dangers to all living organisms. Selecting effective materials for wastewater treatment is vital to restoring a cleaner and more livable environment. Therefore, a photocatalyst material is a material that has a mechanism to eliminate those pollutants. When a photocatalyst absorbs light, typically ultraviolet (UV) or visible light, it excites electrons from the valence band to the conduction band, allowing for chemical reactions such as the degradation of organic pollutants.

Among these photocatalytic semiconductor materials, zinc oxide (ZnO) is considered a semiconductor material that is widely applied for dye degradation because ZnO is a versatile n-type semiconductor with a wide bandgap of approximately 3.37 eV at room temperature [13], which is advantageous for optoelectronic applications, particularly in the UV radiation. This wide bandgap made ZnO a strong UV absorption material, alongside notable transparency and thermal stability. These properties make ZnO particularly useful in applications that demand durability and high performance in extreme conditions, such as optoelectronics [14], [15], transparent conducting oxide [16], [17], gas-

Corresponding Author: 67116001@kmitl.ac.th

sensors [18], [19], solar cells [20], [21], self-powered devices [22], [23], energy storage [24], protective coatings [9] and especially photocatalysts [11], [12].

However, zinc oxide as a material for photocatalytic application still has the limitation of its wide energy band, which may result in inefficient dye degradation reaction and even lead to the termination of the reaction. Therefore, the improvement of dye degradation efficiency by developing Ag NPs decorated-ZnO composites has been studied, but the energy gap band remains wide [25]. The ZnO-M_xO_y heterostructures (M=Co, Mn, Ni, or In) have been fabricated to enhance photocatalytic efficiency, but the composite structure can be distorted from issues such as increased charge recombination within the secondary oxide [26], [27]. Nitrogen-doped zinc oxide (N-doped ZnO) has also been studied to enhance the photocatalytic activity in ultraviolet (UV) and visible light, but the synthesis method is a complex synthesis route [28], as well as the synthesized N-doped ZnO beads via a modified sol–gel technique [29]. W, known as a group IB element, could be one of the good candidate acceptors to adjust the electrical semiconducting property of ZnO from n-type to p-type, a low-cost precursor, and simple. Recently, many studies have reported the enhancement of ZnO by doping other materials, such as tungsten (W), significantly to improve their properties, like photocatalytic performance for dye degradation, particularly in wastewater treatment applications. Tungsten acts as a dopant by substituting for zinc in the ZnO lattice, which introduces new electronic states within the bandgap, thereby modifying the electronic and optical properties of the semiconductor. The introduction of tungsten ions into the ZnO lattice leads to a narrowing of the bandgap or shifting of the band edges [30], which facilitates better absorption of visible light. The ability to utilize a broader spectrum of light makes W-doped ZnO more effective under sunlight or artificial light sources. Moreover, Tungsten doping improves the charge carrier dynamics within the ZnO structure. By generating additional energy levels within the bandgap, tungsten can help to stabilize the electron-hole pairs formed during photocatalytic reactions. This stabilization minimizes the recombination of charge carriers, allowing more electrons and holes to participate in the degradation of dye molecules. The W-doped ZnO has been studied as a highly active photocatalyst toward dye photodegradation of methylene blue in aqueous solution [31]. However, methylene blue is a dye pollutant that has a less complex molecular structure than other dye pollutants like rhodamine B.

In this research, we reported tungsten (W)-doped ZnO nanoparticles synthesized with varying W dopant concentrations via the co-precipitation method to study their physical and optical properties for photocatalysis applications. All as-prepared samples show different morphologies when increasing the W dopant concentrations. Moreover, to evaluate the enhancement in the degradation of rhodamine B as a dye pollutant, all samples were tested using a Xenon lamp as a light source.

2. Experimental

2.1 Materials

Zinc (II) acetate dihydrate ($Zn(CH_3CO_2)_2 \cdot 2H_2O$) and sodium tungstate dihydrate ($Na_2WO_4 \cdot 2H_2O$) were used as starting materials. Deionized water was used as a solvent. Sodium hydroxide (NaOH) was used as a pH adjustment and capping agent. Rhodamine B was used as a model pollutant. All chemicals in this study were analytical grade and used in experiments.

2.2 Preparation of W-doped ZnO particles

For the synthesis of W-doped ZnO particles, Zinc (II) acetate dihydrate (0.02 mol) as a zinc precursor and a certain amount of sodium tungstate dihydrate as a tungsten precursor were dissolved in deionized water (100 mL) at room temperature until dissolved. The solution was then added dropwise 0.1 M NaOH, to adjust pH to 11 for the hydrolysis of Zn^{2+} ions, leading to the formation of $Zn(OH)_2$ precipitates. The reaction mixture was permitted to react for about 2 hours at a constant temperature of 80°C. Thereafter, the samples were separated and washed four times with deionized water. Then, the solids were collected and dried in an oven at 100°C overnight. The final product was calcinated at 600°C for 5 hours to obtain the W-doped ZnO particles, then used for further characterization. The W dopants were meant to create a trap-state in the ZnO structure, narrowing its band gap and improving the photocatalytic performance. The W/Zn mol ratios were 0, 0.01, 0.03, 0.05, and 1.00, and the corresponding samples are denoted as WZ-0, WZ-1, WZ-3, WZ-5, and WZ-10, respectively.

2.3 Photocatalytic testing

Rhodamine B is a synthetic xanthene dye widely used in industries such as textiles, printing, paper, pharmaceuticals, and food production. Since it has a stable aromatic structure and ethyl amino groups, which make it resistant to degradation, serving as a challenging test for evaluating treatment methods, the photocatalytic performance for degrading Rhodamine B (RhB), as an evaluated model pollutant, is evaluated to ensure effective breakdown. The first step involved preparing a 30 mL solution containing 10 µM of RhB, and 0.03 g of W-doped ZnO was added. After the addition of the W-doped ZnO, the mixture was stirred in the dark for 30 minutes to achieve equilibrium in the absorption and desorption processes on the photocatalyst surface. Following this, a 300 W Xenon lamp was activated to provide for the photodegradation process under visible light. The experiment was conducted under these conditions with continuous stirring, and samples were collected every 15 minutes over a total duration of 60 minutes. Once the sample collection was complete, the solution was centrifuged at 5200 rpm for 20 minutes to separate the precipitate from the liquid phase. After centrifugation, the absorbance of the remaining RhB in the solution was analyzed using the Thermo Helios Alpha UV/Vis spectrophotometer. This measurement provided quantitative data on the remaining concentration of Rhodamine B dye, facilitating the assessment of degradation efficiency resulting from the photocatalytic process.

2.4 Characterization

The crystal structure of the synthesized samples was determined by the X-Ray Diffractometer (XRD, Rigaku, SmartLab) equipped with Cu-Kα radiation. The morphology structure and the elemental analysis of the samples were investigated by a Field Emission Scanning Electron Microscope (FE-SEM, JEOL, JEOL JSM-7610F) and an Energy-dispersive X-ray spectroscopy (EDS, FEI, Quanta 250 and JEOL, JEOL JSM-7610F), respectively. The optical property of the samples was measured by a UV-VIS-NIR Spectrophotometer (UV-VIS-NIR, HITACHI, UH4150) in the range of 300-700 nm. The photocatalytic process was monitored using a UV-VIS spectrophotometer (UV-VIS, Thermo, Helios Alpha) with a 300W xenon lamp light source.

3. Result and discussion

3.1 Structure and morphology of W-doped ZnO particles

X-ray diffraction (XRD) patterns of W-doped ZnO particles are shown in Fig. 1. All the samples exhibit typical diffraction of (100), (002), (101), (102), (110), (103), (200), (112), (201), (004), and (202) planes that can be assigned to hexagonal ZnO structure [JCPDS No.01-075-0576]. Meanwhile, increasing W dopants is leading to an obvious XRD peak shift to a higher angle. According to Bragg's law equation, this might be attributed to the substitution of W^{6+} (0.064nm) in the crystal structure, which has a lower ionic radius than Zn^{2+} (0.074nm) since the smaller ions' substitution decreases the lattice spacing of the material [30]. Peaks corresponding to tungsten metal are rarely observed, meaning the lattice structure of ZnO is not changed by tungsten metal dopants, further indicating that tungsten ions were successfully incorporated into the ZnO lattice as dopants. The sharp diffraction peaks indicate that all synthesized W-doped ZnO is highly crystalline. Crystallite size, interplanar distance (d-spacing), and lattice parameter (a, b, c) of W-doped ZnO particles were calculated from the mean of full width at half-maximum (FWHM) of all peaks that occurred according to Bragg's Law, Scherrer, and the hexagonal structure equation, then listed in Table 1. The average crystallite size of all samples is 110–220 Å, indicating that all samples have a nanocrystalline size. As the doping amount of W increased, the average crystallite size was first decreased and then increased. This may be due to the lattice disturbance caused by the W dopant as an impurity in the ZnO crystal structure, which results in a decrease in its crystalline size. Then, when the amount of W dopant is increased, the system starts to undergo aggregation until the good crystal structure is formed again at WZ-5. However, when the amount of W dopant is too high, the excess amount of W ions tends to enter the interstitial sites of the lattice instead of substituting, resulting in the crystallite size of WZ-10 decreasing again [32].

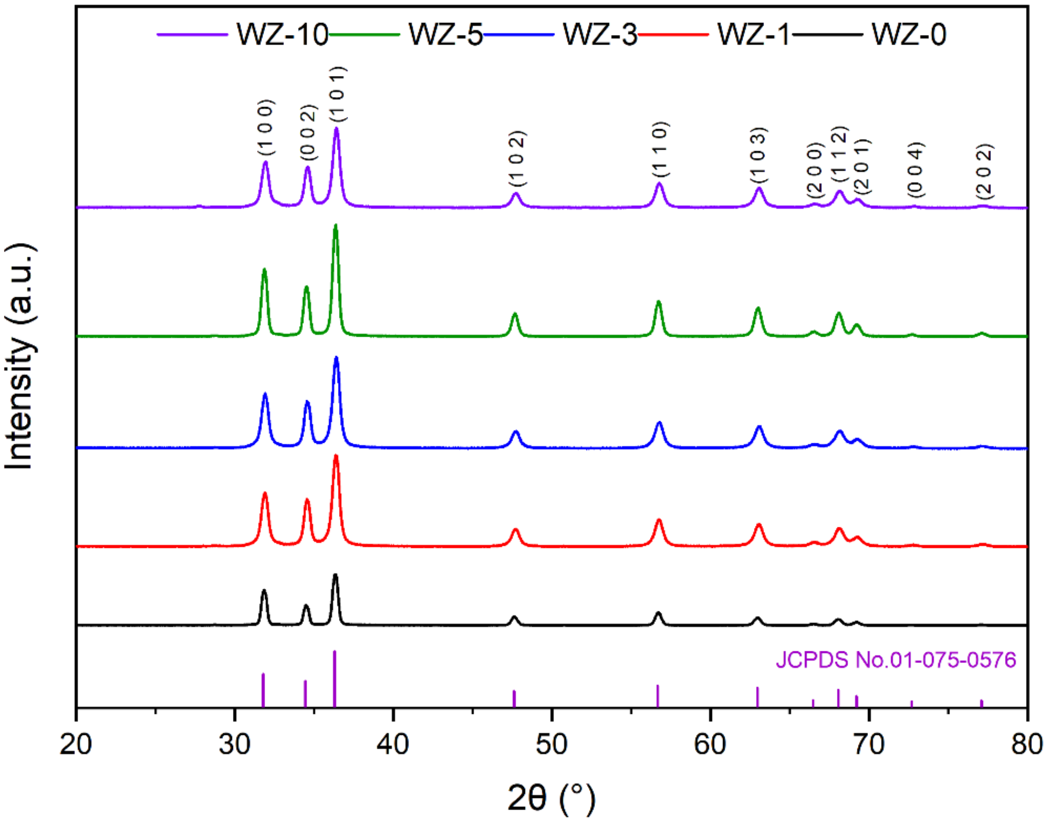

Fig. 1. XRD patterns of ZnO doped with different W doping contents prepared by the co-precipitation process.

Table 1. Crystallite size, interplanar distance (d-spacing), and lattice parameter (a, b, c) of W-doped ZnO particles.

Sample	Crystalline size (Å)	d-spacing (Å)	a = b (Å)	c (Å)
WZ-0	218.39	1.78	3.24	5.19
WZ-1	110.79	1.77	3.24	5.18
WZ-3	149.33	1.77	3.23	5.18
WZ-5	203.44	1.78	3.24	5.19
WZ-10	154.70	1.77	3.23	5.18

FE-SEM photographs with 50,000 times magnification of W-doped ZnO samples are shown in Fig. 2. The micrograph shows that all the samples have particle sizes less than the microscale. Moreover, Fig. 2a revealed that WZ-0 has a clearer circular morphology than other conditions due to its defect-free nature, which enables uniform crystal growth. Compared to Fig. 2b-e, all conditions with W dopants have less circular morphology and more disordered particle size distribution in WZ-1 and WZ-3 before the particle size distribution becomes more uniform at WZ-5, then increases again at WZ-10. This confirmed the interference of W dopant by ZnO crystal growth, which is consistent with the crystal structure analysis. Since WZ-5 has a more uniform particle size distribution than the other conditions, it can be assumed that this condition has an optimized amount of W dopant [33]. Furthermore, the EDS spectra results are presented in Fig. 3. There are only Zn and O elements found in Fig. 3a, indicating that WZ-0 has a pure ZnO structure with no other impurity. As well as in Fig. 3b-e, only Zn, O, and W, whose role as the dopant elements is pointed out, confirming the presence of W dopants in WZ-1, WZ-3, WZ-5, and WZ-10.

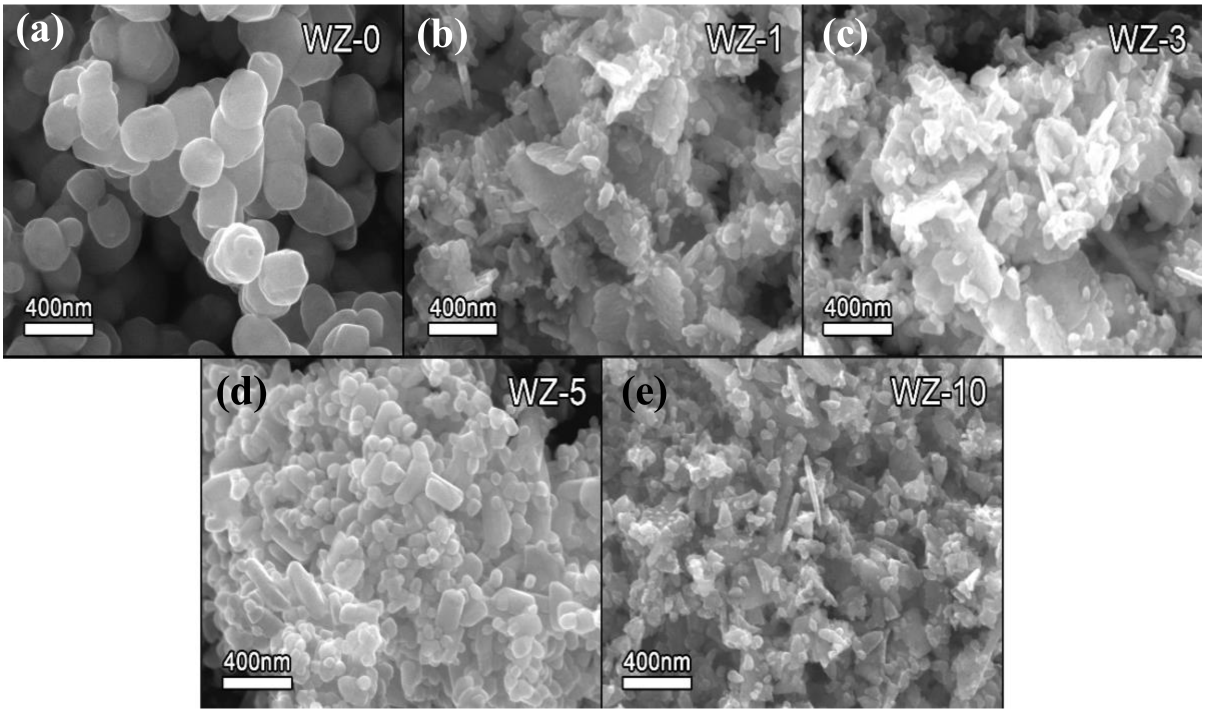

Fig. 2. FE-SEM photographs of W-doped ZnO (a) WZ-0, (b) WZ-1, (c) WZ-3, (d) WZ-5, and (e) WZ-10 particles.

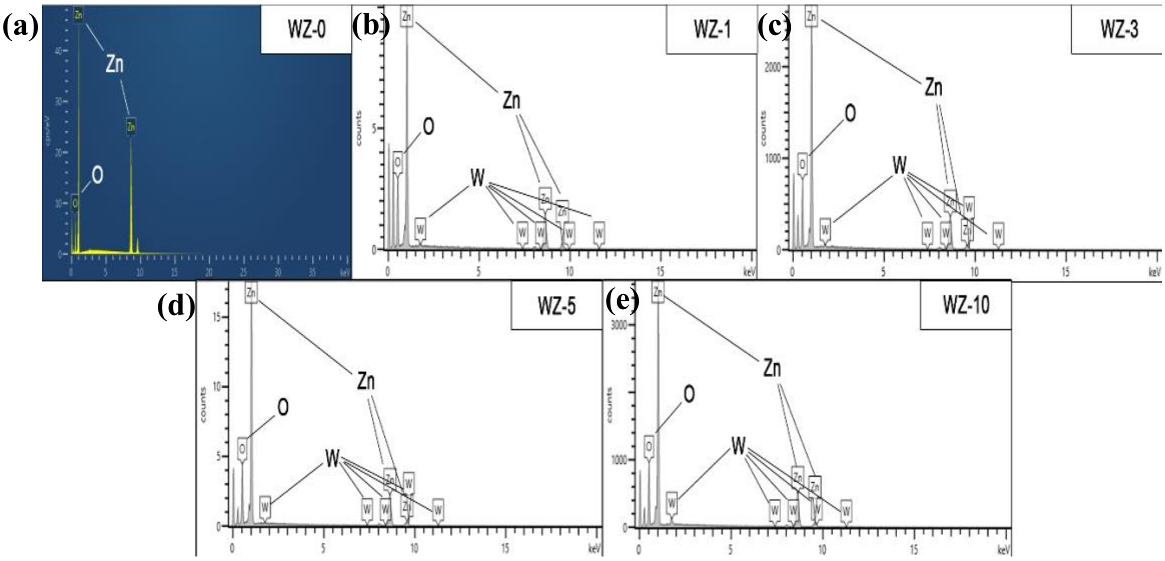

Fig. 3. EDS spectra of W-doped ZnO (a) WZ-0, (b) WZ-1, (c) WZ-3, (d) WZ-5, and (e) WZ-10 particles.

3.2 Optical properties of W-doped ZnO particles

The UV-Vis-NIR diffuse reflectance spectra of W-doped ZnO particles are presented in Fig. 4. All samples exhibited minimal reflection in the ultraviolet spectrum and significant reflection in the visible light spectrum, indicating that all W-doped ZnO particles possess high ultraviolet absorbance capabilities, making them suitable for photocatalytic applications that utilize ultraviolet light as photon energy. Among all conditions, WZ-5 exhibits the largest shift in the reflection edge toward the visible light spectrum, indicating a significant reduction in its band gap energy compared to other samples and an enhanced absorption of lower-energy visible light [32]. For more information, the band gap energy of the samples was calculated using a Kubelka-Munk equation. Fig. 5 shows that the band gap energy of samples firstly decreases as the amount of W dopants increases, then increases at WZ-10, which has the highest amount of W dopants in this research. These results indicate that the appearance of acceptor W dopants in the samples caused the formation of trap states, leading to the decrease of band gap energy [34]. Furthermore, WZ-5 has the smallest band gap energy because of the introduction of defect levels within the band structure due to W^{6+} substitution, which narrows the energy gap between the valence and conduction bands. This band gap narrowing enhances the ability of the material to absorb visible light instead of just ultraviolet light since narrowed band gap can promote an electron excitation with lower-energy photons, enabling the up-conversion process using less energy, allowing WZ-5 to absorb across a broader range of the solar spectrum which should be improving its photocatalytic performance since the creation of electron-hole pair received from electron excitation which role as the important factor to react with the outside molecules was easily generate and making it the most effective sample for Rhodamine B degradation.

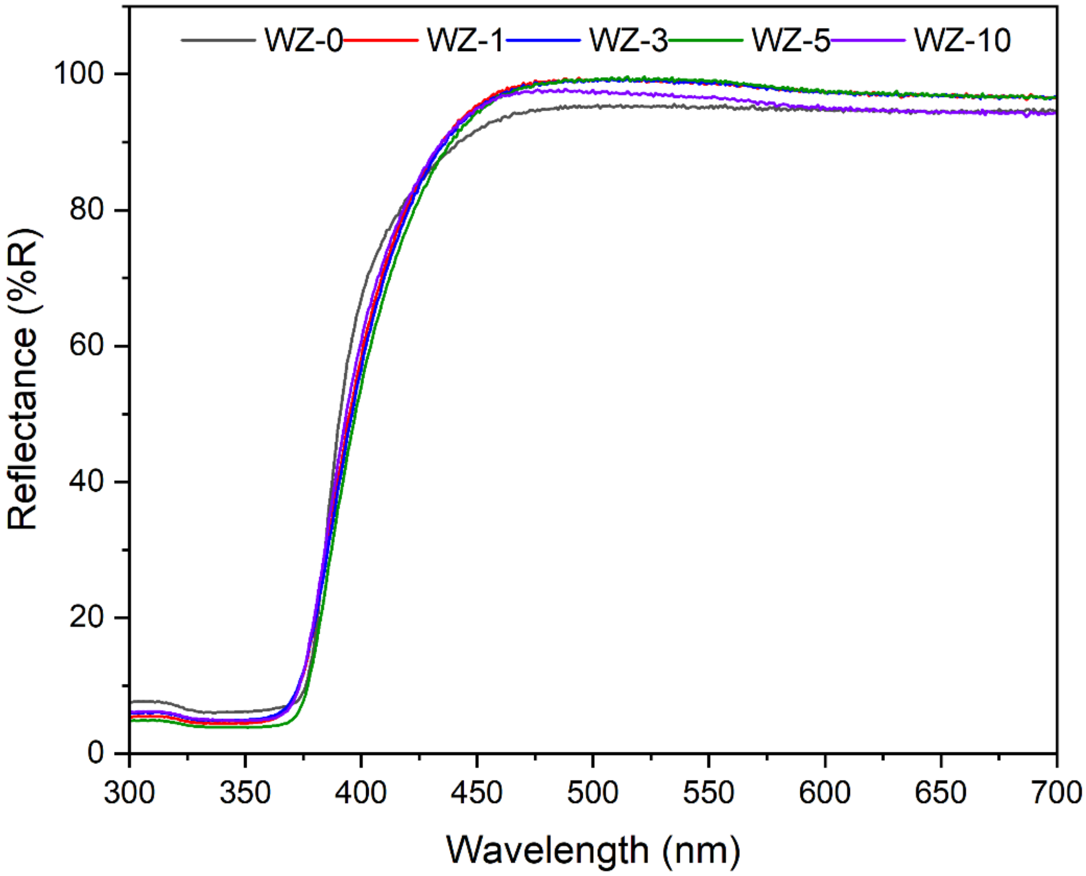

Fig. 4. UV–Vis–NIR diffuse reflectance spectra of ZnO particles doped with different W doping contents.

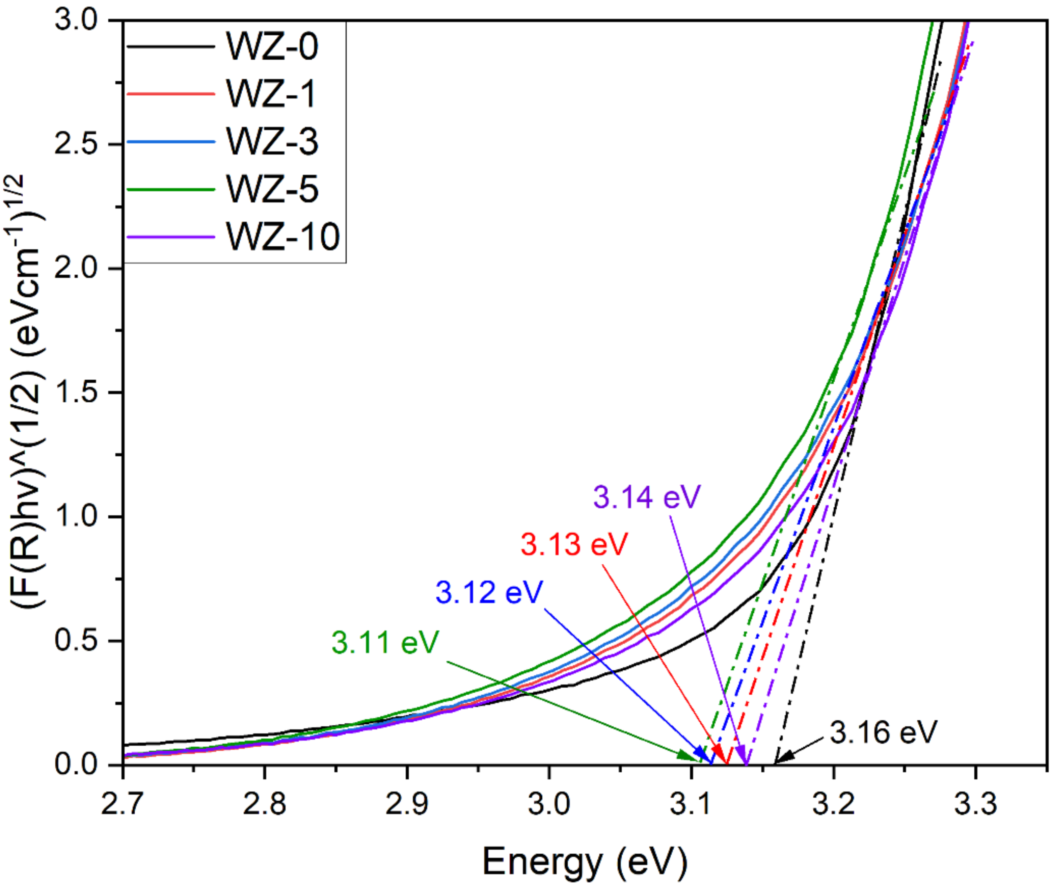

Fig. 5. Band-gap energy of ZnO particles doped with different W doping contents determined based on a direct Kubelka-Munk plot.

3.3 BET Surface area analysis of W-doped ZnO particles

The specific surface areas determined by Brunauer–Emmett–Teller (BET) methods, including nitrogen adsorption/desorption isotherms and pore size distribution, for W-doped ZnO at various doping concentrations are demonstrated in Fig. 6. The characteristic IUPAC classification of adsorption isotherms indicates that all samples are classified as Type IV with H3 hysteresis, which indicates the presence of mesoporous structures formed by non-rigid aggregates or plate-like particles with slit-shaped pores [35]. The H3 type hysteresis loops observed in all samples exhibit variations that may result from the plate-like aggregation [36] of W-doped ZnO particles with increasing W concentrations. Furthermore, the results of BET analysis, including surface area, cumulative volume, and average pore diameter, are presented in Table 2. The average pore diameter for all W-doped ZnO samples ranges from 4.3 to 6.4 nm, corresponding to a mesoporous structure with pore sizes between 2 and 50 nanometers. These results confirm the presence of a conventional mesoporous configuration in all samples, which indicates the efficient diffusion of dye molecules into the material and enhances light absorption due to multiple scattering effects within the porous network. Additionally, the mesoporous structure facilitates charge carrier separation by shortening diffusion paths, thus improving photocatalytic efficiency. Despite the presence of H3-type hysteresis loops, the surface areas do not correlate with the average pore diameter but are influenced by the size and shape of the particles, as discussed in the SEM analysis. The ZnO material with the highest specific surface area was achieved with the WZ-3 sample, due to the mixture of small rod-like and plate-shaped morphologies, which is similar to WZ-1. In contrast, the lowest specific surface area was observed in the WZ-5 sample, likely due to structural changes that caused pore blockage or particle agglomeration, related to the high aggregation of the W-doped ZnO clusters in rod shapes. These results highlight that not only particle shape but also the degree of aggregation have a significant impact on the specific surface area as measured by BET analysis. The highest surface area observed in the WZ-3 sample can be attributed to its mixed rod-like and plate-like morphologies, which offer a greater exposed surface and pore accessibility. In contrast, the lower surface area of WZ-5 is likely a result of particle agglomeration, which reduces the number of accessible pores by blocking them and decreasing the effective surface. According to SEM-observed morphology and BET-measured specific surface area analysis, it can be summarized that a mixture of rod-like and plate-like increases the specific surface area due to its large surface area. In contrast, high aggregation of particles leads the samples, especially WZ-5, to have a small specific surface area compared to the others. So, non-aggregated or irregularly shaped particles provide better porosity and thus higher photocatalytic efficiency. The specific surface area of the WZ-1 sample was comparable to that of the WZ-10 sample, attributed to the mixture of small rod-like ZnO nanostructures. Thus, the isotherms of all samples suggest that each material has a mesoporous structure, as evidenced by the Type IV isotherm and hysteresis, highlighting differences in pore shape, size, and distribution among the samples, which, in turn, affect photocatalytic performance. A higher surface area is crucial for enhancing photocatalytic efficiency since reactions predominantly occur at the material's surface.

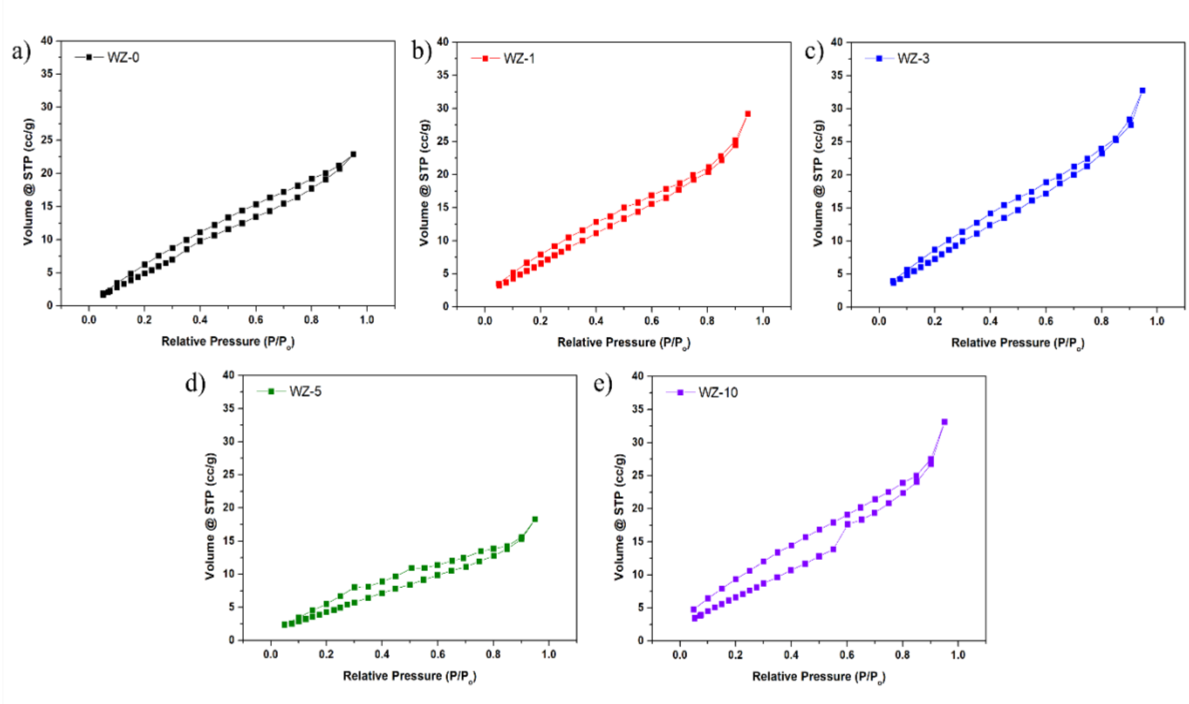

Fig. 6. BET curves of W-doped ZnO with (a) WZ-0, (b) WZ-1, (C) WZ-3, (d) WZ-5, and (e) WZ-10 particles.

Table 2. Results of surface area per volume, cumulative volume, and average pore diameter.

Samples	BET Surface Area (m^2g^{-1})	Cumulative Volume (1–50 nm, cc^3g^{-1})	Average Pore Diameter (nm)
WZ-0	32.95	0.031	4.3
WZ-1	37.80	0.037	4.793
WZ-3	40.42	0.041	5.028
WZ-5	21.49	0.023	5.269
WZ-10	32.06	0.040	6.402

3.4 Photocatalytic properties of W-doped ZnO particles

To investigate how increasing W concentrations in W-doped ZnO particles affect photocatalytic efficiency. The photocatalytic performance of all samples was evaluated by measuring the degradation of Rhodamine B (RhB) dye, targeting the breakdown of organic pollutants under Xenon light irradiation. The photocatalytic activity of the nanocomposite photocatalysts under visible light irradiation, expressed in terms of A/A_0 versus irradiation time, is illustrated in Fig. 7. The degradation rate constant (k) was calculated using the equation $\ln(A/A_0) = -kt$ [37], following the pseudo-first-order rate law. The degradation efficiencies of the RhB solutions subjected to photocatalytic degradation with W-doped ZnO after 60 minutes are presented in Table 3. All samples demonstrated effective photodegradation of RhB within 60 minutes. The pure ZnO sample (WZ-0) exhibited approximately 94% degradation efficiency for RhB dye, while the WZ-5 sample showed an enhanced degradation rate, achieving nearly 98% complete degradation compared to the other samples. WZ-3 and WZ-1 also exhibited similar results, with significant improvements attributed to their plate-like morphologies. In contrast, the WZ-10 condition did not perform well in degrading the dye compared to the other conditions, likely due to the formation of a dense sheet-like structure of tungsten aggregates, which resulted in only 60% degradation. Moreover, the spherical structure of ZnO particles demonstrated superior photocatalytic degradation compared to the sheet structure samples [38]. In summary, the spherical morphology of ZnO particles in WZ-0 and WZ-5 contributes to their superior photocatalytic degradation compared to the aggregated sheet-like structures in WZ-10 is likely due to better surface exposure and reduced charge carrier recombination in the more stable spherical structures, while the dense-layered morphology in WZ-10 limits photocatalytic activity. Additionally, the WZ-5 sample also exhibited the narrowest bandgap at 3.11 eV, reduced from 3.16 eV for WZ-0. This reduction in the bandgap contributes to WZ-5 being the most effective configuration for dye degradation, enhancing light absorption and photocatalytic efficiency according to the mechanisms of W-doped ZnO catalysts in photocatalytic reactions.

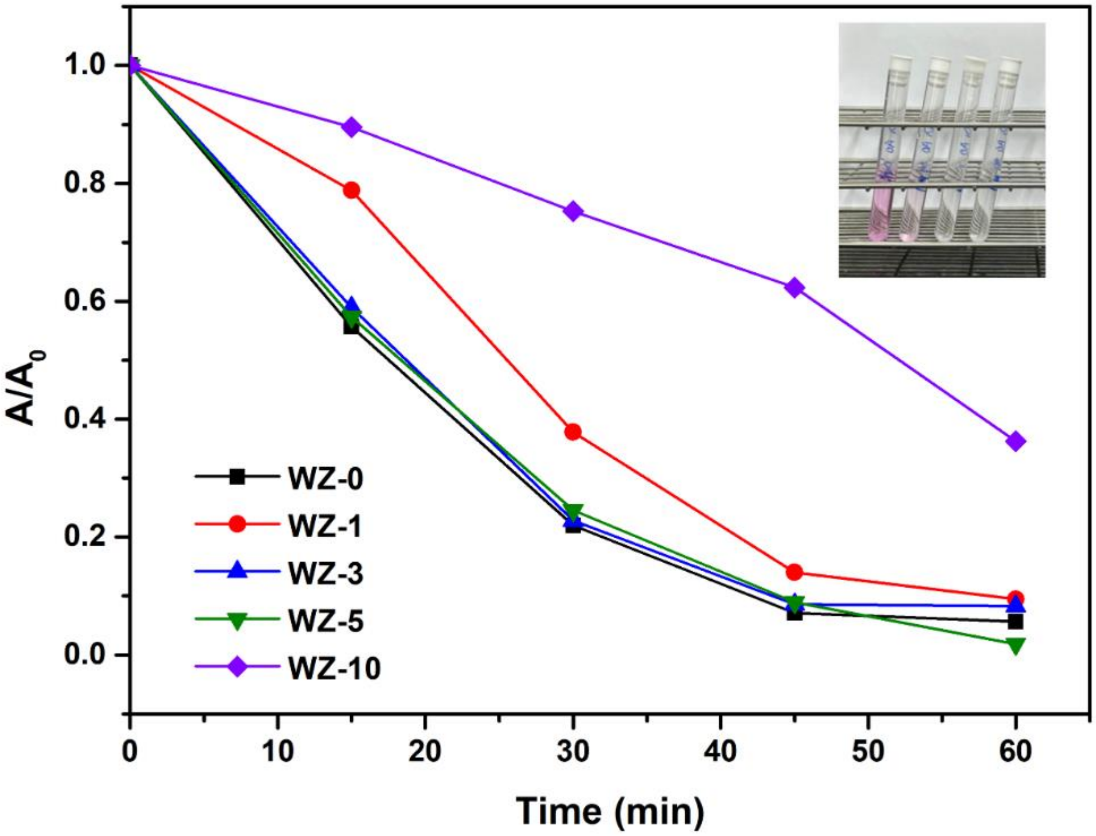

Fig. 7. Photocatalytic activity of all nanocomposite photocatalysts under visible light irradiation in terms of A/A0 and irradiation time.

Table 3. Degradation efficiency and pseudo-first order rate constant for photocatalytic degradation of W-doped ZnO.

Samples	Kinetic constant (K) (min^{-1})	R-squared (R^2)	Degradation efficiency (%)
WZ-0	0.7799	0.9698	94.33
WZ-1	0.6447	0.9655	90.55
WZ-3	0.6919	0.9489	91.74
WZ-5	0.9854	0.9644	98.16
WZ-10	0.2391	0.8969	63.71

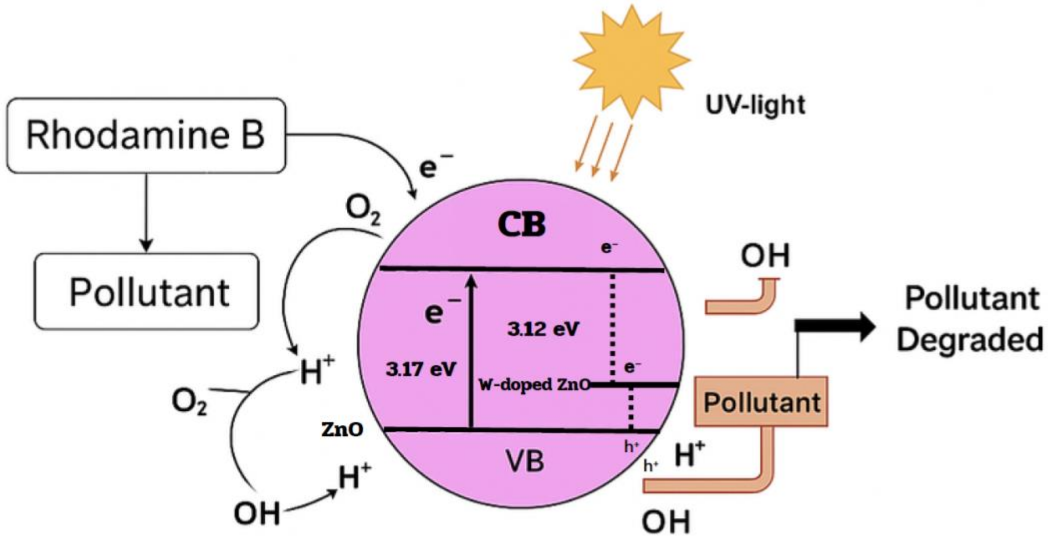

Fig. 8. Photocatalytic activity of all nanocomposite photocatalysts under visible light irradiation in terms of A/A0 and irradiation time.

The mechanisms of W-doped ZnO catalysts in photocatalytic reactions are illustrated in Fig. 8, highlighting the critical roles of superoxide ($\bullet O_2^-$) and hydroxyl radicals ($\bullet OH$) in this process. Once W-doped ZnO catalytically absorbs photon energy from ultraviolet or visible light, since the narrowing band gap can cause an electron excitation with lower-energy photons, electrons from the valence band will be excited to the conduction band, creating electron-hole pairs. Electrons at the conduction band will react with adsorbed oxygen to generate superoxide radicals ($\bullet O_2^-$), while holes in the valence band will oxidize water molecules to produce hydroxyl radicals ($\bullet OH$). Then, both highly reactive oxygen species (ROS) will oxidize pollutant molecules like Rhodamine B and break them down into less harmful substances. Also, trap states created by W dopants act as temporary holding sites for photogenerated electrons or holes, which reduces their immediate recombination and effectively prolongs their lifetimes, which extends the availability of charge carriers and increases the probability of redox reactions occurring at the catalyst surface. The results demonstrate that W-doped ZnO exhibits significantly enhanced photocatalytic activity in degrading RhB compared to pure ZnO. This improved activity is attributed not only to better charge separation but also to the influence of tungsten on the photocatalytic reaction itself. It is essential to determine the optimal concentration of W to effectively separate excitons, which are bound electron-hole pairs, as excessive amounts of W can create additional recombination centers that ultimately degrade photocatalytic activity [30]. Consequently, WZ-5, which has the narrowest band gap due to optimal tungsten dopant, shows a significant enhancement in photocatalytic performance compared to pure ZnO (WZ-0). The incorporation of tungsten ions into the

ZnO lattice narrows the bandgap, allowing the material to absorb visible light and produce electron-hole pairs. Under visible light activation, WZ-5 generates holes that can be directly transferred to the valence band, allowing both materials to absorb UV light and generate electron-hole pairs. Furthermore, the valence band of W-doped is closer to the conduction band of ZnO, facilitating electron transfer from the conduction band of W dopant to the valence band of ZnO, thus increasing the electron population in ZnO. This enhanced electron population allows for more efficient visible light absorption by ZnO, resulting in increased electron-hole pair separation. Therefore, W-doped ZnO can improve electron population, which is primarily responsible for generating superoxide radical, which is the leading species involved in the photolysis of RhB dye under optimal conditions [39]. However, when tungsten dopants exceed the solubility limit and enter interstitial sites within the ZnO lattice, they introduce deep-level trap states in the band gap [40]. These defect sites can capture photo-generated electrons or holes and facilitate their non-radiative recombination, thereby reducing the availability of charge carriers for photocatalytic reactions. This recombination mechanism is a key factor in the diminished photocatalytic activity observed in highly doped samples such as WZ-10.

4. Conclusion

In this study, W-doped ZnO nanoparticles were successfully synthesized via the co-precipitation method. The incorporation of W ions into the hexagonal ZnO lattice influenced morphology, reducing the bandgap energy from 3.16 eV to 3.11 eV, leading to an increase in photocatalytic performance, especially in the visible light region. Among all synthesized samples, WZ-5 demonstrated the most favorable properties, exhibiting a highly crystalline, high particle size distribution, and the largest amount of bandgap narrowing due to the optimal molar dopant of W. These characteristics contributed to its superior photocatalytic performance, achieving a 98.16% degradation efficiency of Rhodamine B under visible light irradiation. The enhanced activity can be attributed to more effective charge separation that occurred from the W dopants' trapped state, leading to the reduced recombination of charge carriers and improved light absorption. This indicates that W-doping is a promising strategy for enhancing the photocatalytic efficiency of ZnO-based materials for wastewater treatment applications.

Acknowledgments

This research was conducted at King Mongkut’s Institute of Technology Ladkrabang. The authors would like to thank Nanocomposite Materials Research Laboratory (NMRL), School of Integrated Innovative Technology (SIITec), and King Mongkut’s Institute of Technology Ladkrabang (KMITL) for the laboratory research.

References

[1] Zhou, W., Zou, X., Najmaei, S., Liu, Z., Shi, Y., Kong, J., Lou, J., Ajayan, P. M., Yakobson, B. I., & Idrobo, J. (2013). Intrinsic Structural Defects in Monolayer Molybdenum Disulfide. *Nano Letters*, *13*(6), 2615–2622. DOI: 10.1021/nl4007479.

[2] Yan, F., Zhao, L., Patanè, A., Hu, P., Wei, X., Luo, W., Zhang, D., Lv, Q., Feng, Q., Shen, C., Chang, K., Eaves, L., & Wang, K. (2017). Fast, multicolor photodetection with graphene-contacted *p*-GaSe/*n*-InSe van der Waals heterostructures. *Nanotechnology, 28*(27), 27LT01. DOI: 10.1088/1361-6528/aa749e.

[3] Protesescu, L., Yakunin, S., Bodnarchuk, M. I., Krieg, F., Caputo, R., Hendon, C. H., Yang, R. X., Walsh, A., & Kovalenko, M. V. (2015). Nanocrystals of Cesium Lead Halide Perovskites ($CsPbX_3$, X = Cl, Br, and I): Novel Optoelectronic Materials Showing Bright Emission with Wide Color Gamut. *Nano Letters, 15*(6), 3692–3696. DOI: 10.1021/nl5048779.

[4] Baugher, B. W. H., Churchill, H. O. H., Yang, Y., & Jarillo-Herrero, P. (2014). Optoelectronic devices based on electrically tunable p–n diodes in a monolayer dichalcogenide. *Nature Nanotechnology, 9*(4), 262–267. DOI: 10.1038/nnano.2014.25.

[5] Yuan, J., Zhang, Y., Zhou, L., Zhang, G., Yip, H., Lau, T., Lu, X., Zhu, C., Peng, H., Johnson, P. A., Leclerc, M., Cao, Y., Ulanski, J., Li, Y., & Zou, Y. (2019). Single-Junction Organic Solar Cell

with over 15% Efficiency Using Fused-Ring Acceptor with Electron-Deficient Core. *Joule, 3*(4), 1140–1151. DOI: 10.1016/j.joule.2019.01.004.

[6] Varadwaj, A., Varadwaj, P. R., & Yamashita, K. (2017). Revealing the Chemistry between Band Gap and Binding Energy for Lead-/Tin-Based Trihalide Perovskite Solar Cell Semiconductors. *ChemSusChem, 11*(2), 449–463. DOI: 10.1002/cssc.201701653.

[7] Wu, R., Tian, L., Li, H., Liu, H., Luo, J., Tian, X., Hua, Z., Wu, Y., & Fan, S. (2022). A selective methane gas sensor based on metal oxide semiconductor equipped with an on-chip microfilter. *Sensors and Actuators B Chemical, 359*, 131557. DOI: 10.1016/j.snb.2022.131557.

[8] Hua, Z., Li, Y., Zeng, Y., & Wu, Y. (2017). A theoretical investigation of the power-law response of metal oxide semiconductor gas sensors I: Schottky barrier control. *Sensors and Actuators B Chemical, 255*, 1911–1919. DOI: 10.1016/j.snb.2017.08.206.

[9] Han, C., Wang, F., Gao, C., Liu, P., Ding, Y., Zhang, S., & Yang, M. (2015). Transparent epoxy–ZnO/CdS nanocomposites with tunable UV and blue light-shielding capabilities. *Journal of Materials Chemistry C, 3*(19), 5065–5072. DOI: 10.1039/c4tc02880e.

[10] Baimanova, R., Luo, F., & Yang, M. (2022). Preparation of Iron-Doped Titania Nanoparticles and Their UV-Blue Light-Shielding Capabilities in Polyurethane. *Materials, 15*(20), 7370. DOI: 10.3390/ma15207370.

[11] Wang, B., Wang, X., Lu, L., Zhou, C., Xin, Z., Wang, J., Ke, X., Sheng, G., Yan, S., & Zou, Z. (2017). Oxygen-Vacancy-Activated CO_2 Splitting over Amorphous Oxide Semiconductor Photocatalyst. *ACS Catalysis, 8*(1), 516–525. DOI: 10.1021/acscatal.7b02952.

[12] Wu, G., & Xing, W. (2018). Fabrication of ternary visible-light-driven semiconductor photocatalyst and its effective photocatalytic performance. *Materials Technology, 34*(5), 292–300. DOI: 10.1080/10667857.2018.1553267.

[13] Sinornate, W., & Chongsri, K. (2019). Preparation and Characterization of Ag-doped ZnO thin film deposited by sol-gel-based coating method. *Thai Journal of Nanoscience and Nanotechnology, 4*(1), 20–24. http://www.nano.kmitl.ac.th/tjnn/index.php/tjnn/article/view/35.

[14] Ali, G. A., Emam-Ismail, M., El-Hagary, M., Shaaban, E., Moustafa, S., Amer, M., & Shaban, H. (2021). Optical and microstructural characterization of nanocrystalline Cu doped ZnO diluted magnetic semiconductor thin film for optoelectronic applications. *Optical Materials, 119*, 111312. DOI: 10.1016/j.optmat.2021.111312.

[15] Hu, H., Xiong, Z., Kang, C., Cui, Y., & Chen, L. (2022). Hydroxyl-functionalized ZnO monolayers for optoelectronic devices: Atomic structures and electronic properties. *Vacuum, 208*, 111721. DOI: 10.1016/j.vacuum.2022.111721.

[16] Bouaine, A., Bourebia, A., Guendouz, H., & Riane, Z. (2018). Synthesis and characterization of In doped ZnO thin film as efficient transparent conducting oxide candidate. *Optik, 166*, 317–322. DOI: 10.1016/j.ijleo.2018.04.017.

[17] Liu, H., Li, H., Tao, J., Liu, J., Yang, J., Li, J., Song, J., Ren, J., Wang, M., Yang, S., Song, X., & Wang, Y. (2023). Single Crystalline Transparent Conducting F, Al, and Ga Co-Doped ZnO Thin Films with High Photoelectrical Performance. *ACS Applied Materials & Interfaces, 15*(18), 22195–22203. DOI: 10.1021/acsami.2c22784.

[18] Rodlamul, P., Tamura, S., & Imanaka, N. (2019). Effect of p- or n-Type Semiconductor on CO Sensing Performance of Catalytic Combustion-Type CO Gas Sensor with CeO_2-ZrO_2-ZnO Based Catalyst. *Bulletin of the Chemical Society of Japan, 92*(3), 585–591. DOI: 10.1246/bcsj.20180284.

[19] Han, T., Bak, S., Kim, S., Lee, S. H., Han, Y., & Yi, M. (2021). Decoration of CuO NWs Gas Sensor with ZnO NPs for Improving NO_2 Sensing Characteristics. *Sensors, 21*(6), 2103. DOI: 10.3390/s21062103.

[20] Minami, T., Miyata, T., & Nishi, Y. (2014). Cu_2O-based heterojunction solar cells with an Al-doped ZnO/oxide semiconductor/thermally oxidized Cu_2O sheet structure. *Solar Energy*, *105*, 206–217. DOI: 10.1016/j.solener.2014.03.036.

[21] Tubtimtae, A., Arthayakul, K., Teekwang, B., Hongsith, K., & Choopun, S. (2013). MnTe semiconductor-sensitized boron-doped TiO_2 and ZnO photoelectrodes for solar cell applications. *Journal of Colloid and Interface Science*, *405*, 78–84. DOI: 10.1016/j.jcis.2013.05.038.

[22] Zhou, X., Xu, J., Shi, S., Chen, J., Xu, J., Kong, L., Zhang, X., & Li, L. (2023). Self-powered dual-wavelength polarization-sensitive photodetectors based on ZnO/$BiFeO_3$ heterojunction. *Applied Surface Science*, *623*, 157032. DOI: 10.1016/j.apsusc.2023.157032.

[23] Saha, R., Dalapati, G. K., Chakrabarti, S., Karmakar, A., & Chattopadhyay, S. (2022). Yttrium (Y) doped ZnO nanowire/p-Si heterojunction devices for efficient self-powered UV-sensing applications. *Vacuum*, *202*, 111214. DOI: 10.1016/j.vacuum.2022.111214.

[24] Oliveira, D. A., Da Silva, R. A., Orlandi, M. O., & Siqueira, J. R. (2022). Supercapacitor Based on Nanostructured Multilayer Films Consisting of Polyelectrolyte/Graphene Oxide-MnO_2-ZnO for Energy Storage Applications. *Physica Status Solidi (A) Applications and Materials Science*, *219*(23). DOI: 10.1002/pssa.202100871.

[25] Dangsaart, B., Boonyarattanakalin, K., Bangbai, C., Sungthong, A., & Chongsri, K. (2024). Enhanced optical and photocatalytic properties of Ag NPs decorated-ZnO composites. *Thai Journal of Nanoscience and Nanotechnology, 9*(2), 1–10. https://ph05.tci-thaijo.org/index.php/TJNN/article/view/142.

[26] Nayan, M. B., Jagadish, K., Abhilash, M. R., Namratha, K., & Srikantaswamy, S. (2019). Comparative Study on the Effects of Surface Area, Conduction Band and Valence Band Positions on the Photocatalytic Activity of ZnO-M_xO_y Heterostructures. *Journal of Water Resource and Protection, 11*(03), 357–370. DOI: 10.4236/jwarp.2019.113021.

[27] Abhivyakti, N., Kaur, P., Aggarwal, D., Nitansh, N., & Singhal, S. (2025). Defect-engineered C,N-ZnO/Co_3O_4/$CoFe_2O_4$/Fe_3O_4 for ultra-fast tetracycline degradation and environmental impact assessment using an in silico mathematical model. *Advanced Composites and Hybrid Materials*, *8*(1). DOI: 10.1007/s42114-025-01230-3.

[28] Tang, C., Chen, C., Zhang, H., Zhang, J., & Li, Z. (2020). Enhancement of degradation for nitrogen doped zinc oxide to degrade methylene blue. *Physica B Condensed Matter*, *583*(43), 412029. DOI: 10.1016/j.physb.2020.412029.

[29] Mandor, H., Amin, N. K., Abdelwahab, O., & El-Ashtoukhy, E. Z. (2022). Preparation and characterization of N-doped ZnO and N-doped TiO_2 beads for photocatalytic degradation of phenol and ammonia. *Environmental Science and Pollution Research*, *29*(37), 56845–56862. DOI: 10.1007/s11356-022-19421-6.

[30] Russo, M., Iervolino, G., & Vaiano, V. (2021). W-Doped ZnO photocatalyst for the degradation of glyphosate in aqueous solution. *Catalysts*, *11*(2), 234. DOI: 10.3390/catal11020234.

[31] Moafi, H. F., Zanjanchi, M. A., & Shojaie, A. F. (2013). Tungsten-doped ZnO nanocomposite: Synthesis, characterization, and highly active photocatalyst toward dye photodegradation. *Materials Chemistry and Physics*, *139*(2–3), 856–864. DOI: 10.1016/j.matchemphys.2013.02.044.

[32] Munna, N., Abdur, R., Islam, R., Bashar, M. S., Farhad, S. F. U., Kamruzzaman, M., Aziz, S., Shaikh, M. a. A., Hossain, M., & Jamal, M. S. (2023). Influence of Sn doping on the optoelectronic properties of ZnO nanoparticles. *Nanoscale Advances*, *5*(18), 4996–5004. DOI: 10.1039/d3na00409k.

[33] Ghica, D., Vlaicu, I. D., Stefan, M., Maraloiu, V. A., Joita, A. C., & Ghica, C. (2019). Tailoring the dopant distribution in ZnO:Mn Nanocrystals. *Scientific Reports*, *9*(1). DOI: 10.1038/s41598-019-43388-z.

[34] Abebe, B., Gupta, N. K., & Tsegaye, D. (2024). A critical mini-review on doping and heterojunction formation in ZnO-based catalysts. *RSC Advances*, *14*(25), 17338–17349. DOI: 10.1039/d4ra02568g.

[35] Pal, U., Kim, C. W., Jadhav, N. A., & Kang, Y. S. (2009). Ultrasound-Assisted Synthesis of Mesoporous ZnO Nanostructures of Different Porosities. *The Journal of Physical Chemistry C*, *113*(33), 14676–14680. DOI: 10.1021/jp904377n.

[36] Yurdakal, S., Garlisi, C., Özcan, L., Bellardita, M., & Palmisano, G. (2019). (Photo)catalyst Characterization Techniques: Adsorption Isotherms and BET, SEM, FTIR, UV–Vis, Photoluminescence, and Electrochemical Characterizations. In Marcì, G., & Palmisano, L. (Eds), *Heterogeneous Photocatalysis* (pp. 87–152). Elsevier. DOI: 10.1016/b978-0-444-64015-4.00004-3.

[37] Verma, G., Islam, M., & Gupta, A. (2025). ZnO nanowire-decorated 3D printed pyrolytic carbon for solar light–driven photocatalytic degradation of wastewater contaminants. *Advanced Composites and Hybrid Materials*, *8*(1). DOI: 10.1007/s42114-024-01125-9.

[38] Selvam, N. C. S., Vijaya, J. J., & Kennedy, L. J. (2012). Effects of morphology and ZR doping on structural, optical, and photocatalytic properties of ZnO nanostructures. *Industrial & Engineering Chemistry Research*, *51*(50), 16333–16345. DOI: 10.1021/ie3016945.

[39] Ghazal, S., Mirzaee, M., & Darroudi, M. (2024). Role of Zinc-doped Tungsten Oxide Nanosheets in Photo-catalytic, Anti-Cancer, and antibacterial Applications. *Environmental Technology & Innovation*, *36*, 103908. DOI: 10.1016/j.eti.2024.103908.

[40] Han, D., Du, M., Dai, C., Sun, D., & Chen, S. (2017). Influence of defects and dopants on the photovoltaic performance of Bi_2S_3: first-principles insights. *Journal of Materials Chemistry A*, *5*(13), 6200–6210. DOI: 10.1039/c6ta10377d.